# Study of the proton arc spreading effect on primary ionization rates

Xiaohua Fang, Michael W. Liemohn, and Janet U. Kozyra
Space Physics Research Laboratory, University of Michigan, Ann Arbor, Michigan, USA

Stanley C. Solomon
High Altitude Observatory, National Center for Atmospheric Research, Boulder, Colorado, USA

Received 22 November 2004; revised 22 April 2005; accepted 29 April 2005; published 13 July 2005.

[1] We investigate the influence of the spatial spreading effect in a proton arc with finite width on resulting primary ionization rates, using our three-dimensional (3-D) Monte Carlo ion transport model. By the direct impact from energetic protons and generated hydrogen atoms, ambient neutrals in the Earth's upper atmosphere can be ionized in charge exchange or ionization collisions. The model results show that the ionization rates (and particle fluxes) depend on all of the parameters we varied: incident proton arc dimensions, energy spectra, average energies, latitudinal energy flux distributions, and magnetic field dip angles. It is found that a correction factor, often introduced at an equilibrium altitude (~300 km) in one-dimensional (1-D) theoretical models, cannot completely account for the beam spreading effect for an incident proton arc of finite width. Below ~300 km, ionization rates in 1-D models are generally overestimated at high altitudes (above ~150 km) and underestimated at low altitudes (below ~150 km). The overestimation is caused by overlooking the difference between the spatial spreading for the particle fluxes and for the ionization rates. At low altitudes, the beam radius gets smaller, causing underestimation in the 1-D ionization rates. The results of our 3-D sensitivity study of various parameters can be applied in future studies of auroral and ring current proton precipitation into the upper atmosphere.

**Citation:** Fang, X., M. W. Liemohn, J. U. Kozyra, and S. C. Solomon (2005), Study of the proton arc spreading effect on primary ionization rates, *J. Geophys. Res.*, *110*, A07302, doi:10.1029/2004JA010915.

## 1. Introduction

[2] It has been well established that sometimes at some locations, precipitating protons can be a significant or dominant energy source to the ionosphere-thermosphere system [*Sharber*, 1981; *Gussenhoven et al.*, 1987; *Hardy et al.*, 1989]. It is crucial to consider the role of incident protons in addition to electrons in ionospheric disturbances at auroral latitudes [*Galand and Richmond*, 2001; *Galand et al.*, 2001, and references therein]. Major difficulties in modeling proton precipitation arise because proton and hydrogen atom transport are coupled together through charge exchange and electron stripping collisions within the incident proton beam. These collision processes quickly convert the incident proton beam into a mixture of ions and neutrals. Energetic neutrals in the beam are able to travel across field lines until they are converted through collisions back into ions producing a spatial spreading effect unique to ion precipitation. The spatial spreading poses an additional difficulty for understanding the aeronomical effects of the ion precipitation.

Copyright 2005 by the American Geophysical Union.
0148-0227/05/2004JA010915

[3] *Davidson* [1965] numerically studied the spreading effect and found that particles may move as far as 300 km away from the location of the incident beam. His findings attracted considerable attention as the first demonstration of the significance of spatial spreading. However, these results are best regarded as qualitative because of the coarse atmosphere profiles and collision cross sections used in his Monte Carlo model. In addition, *Davidson* [1965] considered a fine proton beam incident at one point rather than an arc. Although the study yielded physical insights, in reality, a proton aurora has a two-dimensional topside spatial distribution. Thus, the results obtained by *Davidson* [1965] are difficult to directly apply to observations.

[4] *Johnstone* [1972] derived an analytic expression for the spatial spreading of a fine proton beam. It was assumed that the particle spreading scale is determined by the path lengths of protons after the first electron capture. *Igelesias and Vondrak* [1974] then applied and extended the results of *Johnstone* [1972] to study the angular distribution and flux intensity diffusion for a uniform auroral proton arc. The comparison to the numerical simulation results from three dimensional Monte Carlo models [*Lorentzen*, 2000; *Fang et al.*, 2004] verified the key role of the first charge exchange collision in beam spreading. The analytic methods have the advantage of clarifying the physical processes involved.

However, the intrinsic simplifications of these analytic approaches impose certain limitations on their accuracy and on their application in the much more complicated real world.

[5] The transverse spatial spreading effect for a proton arc with finite width has been taken into account in several well-known one-dimensional proton aurora transport models [e.g., *Jasperse and Basu*, 1982; *Galand et al.*, 1997]. Corrections from the particle scattering were made in these 1-D models through an estimated attenuation coefficient $\varepsilon < 1$ multiplying the central fluxes at an equilibrium altitude (around 300 km). The correction factor $\varepsilon$ is calculated from the ratio of the central total proton and hydrogen atom fluxes at the equilibrium altitude to the topside proton impact. The energy loss at high altitudes ($>\sim$300 km) was neglected. Because of the frequent charge exchange/electron stripping collisions, there is no further lateral dispersion below $\sim$300 km. A plane-parallel geometry was assumed at low altitudes.

[6] Instead of making such simplifications, 3-D Monte Carlo techniques have the advantage of simulating the multi-dimensional particle transport process in a natural way. *Kozelov* [1993] developed a Monte Carlo model and investigated the altitude dependence of the beam radii for an incident fine proton beam. The beam spreading effect was also discussed by *Synnes et al.* [1998] and *Lorentzen* [2000] using a Monte Carlo technique. Very recently, *Fang et al.* [2004] set up a Monte Carlo model and extensively examined the transverse spreading effect for both a proton beam at an injection point and a proton arc of longitudinal and latitudinal extent at the top of the atmosphere. The beam spreading was well illustrated over horizontal planes as it evolves in altitude. It was found that the main dispersion region for a proton beam was in the altitude range of around 250–450 km. The effective beam radius, within which 80% of the quantities are confined, was different for particle fluxes and for ionization rates. For a proton arc, attenuation coefficients $\varepsilon$ at 300 km altitude were calculated based on the relative intensities of particle fluxes to the topside injection and were compared to the results of *Igelesias and Vondrak* [1974] and *Jasperse and Basu* [1982]. It was the first time ionospheric disturbances were calculated for a proton arc with finite dimensions. Note that not all Monte Carlo codes have the capability of simulating horizontal diffusion for an incident energetic proton beam. The beam spreading effect is neglected in 1-D codes [e.g., *Solomon*, 2001]. The study undertaken here can be only carried out with a 3-D model.

[7] The proton precipitation problem has received much attention in the literature. However, for those studies employing 1-D models [*Jasperse and Basu*, 1982; *Basu et al.*, 1987; *Galand et al.*, 1997], there is still a lack of knowledge on how well they work to predict ionization rates even after the introduction of a correction factor $\varepsilon < 1$ for the spreading effect inside a proton arc with finite width. *Decker et al.* [1996] compared the results of a numerical solution of the linear transport equations [*Basu et al.*, 1993], an implementation of the continuous slowing-down approximation [*Decker et al.*, 1996, appendix], and a Monte Carlo model [*Kozelov and Ivanov*, 1992], and found very close agreement. Unfortunately, the lateral spreading effect was switched off in the comparison. The accuracy of 1-D models actually has not ever been examined in a quantitative manner when the beam spreading effect has to be considered for an incident proton arc with finite width. This is of importance in understanding electrical conductances and Joule heating and thus the electrodynamics in the thermosphere-ionosphere system, since 1-D models are commonly used in these studies [e.g., *Galand et al.*, 1999, 2001].

[8] In this paper, we utilize a 3-D Monte Carlo proton transport method [*Fang et al.*, 2004] to investigate the errors in ionization rates by 1-D models, where the transverse spreading effect is approximated by introducing a correction factor $\varepsilon < 1$ at an equilibrium altitude. In section 2, we briefly describe the Monte Carlo model used. Section 3 presents the results of a sensitivity study of various parameters, and compares to the 1-D calculation results at the center of a proton arc. A number of topside boundary conditions were used to provide a robust collection of the resulting ionization rates that might be of some use in future studies of auroral and ring current proton precipitation into the upper atmosphere. Two types of incident energy flux spatial distributions with magnetic latitude are imposed, homogeneous and Gaussian. The spreading effect is numerically simulated with either vertical or tilted parallel magnetic field lines. In general, ionization rates in 1-D models are overestimated at high altitudes (above $\sim$150 km) and underestimated at low altitudes (below $\sim$150 km). The sources of the error by 1-D models are extensively discussed in section 4. Finally, the paper's findings are summarized in section 5.

## 2. Three-Dimensional Monte Carlo Model

[9] We use the three-dimensional Monte Carlo model described by *Fang et al.* [2004]. This code tracks the trajectories and energy degradation of incident energetic protons during collisions with ambient neutral particles down to an assigned low energy cutoff limit of 20 eV. A full three-species atmosphere (O, $N_2$, $O_2$) is specified by the Mass Spectrometer and Incoherent Scatter model (MSIS-90) [*Hedin*, 1991]. A variety of effects due to inelastic (charge exchange/electron stripping, ionization, excitation) and elastic collisions are accumulated over the course of the particle traveling in the Earth's atmosphere. An important quantity describing the proton-hydrogen energy deposition is the ionization rate, defined as the number of ionized ambient neutrals per unit volume per unit time in charge exchange and ionization collisions by the direct impact from energetic protons and generated hydrogen atoms. Unless explicit specification is made, the term "ionization" in this paper refers to both charge exchange and ionization collisions. As justified by *McNeal and Birely* [1973], the differential cross sections involving protons and H atoms are very strongly peaked in the forward direction for incident energies above a few hundred electron volts. A forward scattering approximation is thus used in our model for inelastic collisions. As for elastic scattering, the collisional angular redistribution is calculated following the work by *Kallio and Barabash* [2001].

[10] In Figure 10 of *Fang et al.* [2004], primary ionization rates from our 3-D Monte Carlo model were compared to those from a 1-D Monte Carlo model [*Solomon*, 2001]

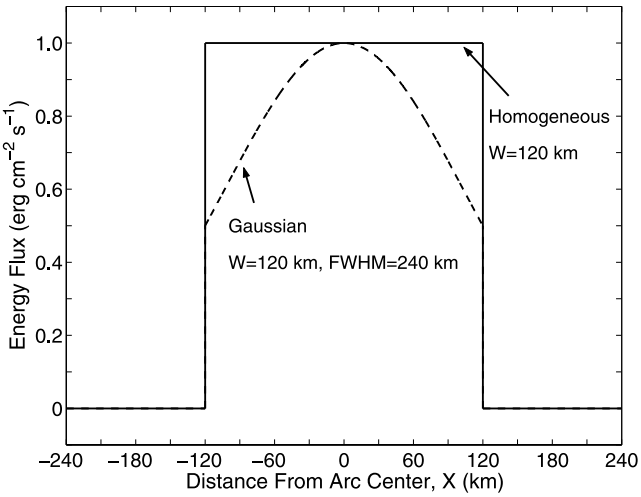


**Figure 1.** Incident proton energy flux versus latitudinal distance away from an arc center. The solid curve is a homogeneous distribution with latitudinal semiwidth $W$ = 120 km. The dashed curve is a Gaussian distribution with $W$ = 120 km and $FWHM$ = 240 km.

and a 1-D multi-stream model [*Galand et al.*, 1997]. The three sets of results agree remarkably well. However, the comparison was made in the context of 1-D transport. That is, the lateral spreading in the incident proton beam was neglected. In this paper we are interested in exploring the error of ionization rates in 1-D models if the beam spreading effect is taken into account for a proton arc with finite width. Therefore we adopt the same atmosphere here to recalculate the ionization profile with the spatial spreading effect considered, and compare again the results between our 3-D Monte Carlo model and 1-D models. The MSIS-90 parameters used were $F_{10.7}$ = 289, $\langle F_{10.7} \rangle$ = 209, a daily $A_P$ of 15, geographic coordinates of 65°N, 160°W, and a time of 0000 UT on 30 January 1985. The flux at the top boundary (950 km) has an incident isotropic pitch angle distribution.

[11] Following the linear transport method [*Jasperse and Basu*, 1982; *Basu et al.*, 1993], we model the geomagnetic field as uniform. The magnetic mirroring effect is neglected in the incident proton beam. The magnetic field lines are parallel to the $X - Z$ plane, where $X$ is pointing northward and $Z$ is directed vertically upward. Two magnetic field geometries are considered: vertical and tilted field lines. In the tilted case, magnetic field lines are tilted toward the positive $X$ direction while pointing downward. We assumed a proton auroral arc of infinite extent in the east-west direction ($Y$) and of semiwidth $W$ in the north-south direction ($X$). In practice, we used a finite value, 1000 km, to approximate the arc semilength in the $Y$ direction, which is sufficiently larger than the arc semiwidth $W$ in the $X$ direction ($W$ ranges from 30 to 120 km in our studies). Unless specified explicitly, an incident Maxwellian energy spectrum is used at the top boundary. Incident energy flux distributions and energy spectra are held constant in the $Y$ direction. In numerical calculations, particles are tracked wherever they go. There is no limitation on the horizontal extent. All results are taken from the $Y$ = 0 plane.

[12] Two different $X$-direction (latitudinal) distributions are imposed at the top boundary in the numerical simulations. The first is a homogeneous energy flux injection,

$$Q_{homo}(X) = \begin{cases} 1, & if\ |X - X_0| \le W \\ 0, & others \end{cases} \quad (1)$$

where $X_0$ is the position of an arc center in the latitudinal direction. While such a distribution is good for illustrative purposes, it may not characterize a real auroral proton arc very satisfactorily. It was observed that the latitudinal dependence is sometimes better approximated by a Gaussian distribution [*Sharber*, 1981],

$$Q_{gaus}(X) = \begin{cases} 2^{-\left(\frac{2(X-X_0)}{FWHM}\right)^2}, & if\ |X - X_0| \le W \\ 0, & others \end{cases} \quad (2)$$

where $FWHM$ is the full width at half maximum for an energy flux distribution. For the purpose of comparison and future application, the simulation results have been scaled to an incident energy flux of $Q_0$ = 1 erg cm$^{-2}$ s$^{-1}$ at the center of the arc. Figure 1 presents examples of how energy fluxes from these two distribution functions vary with latitudinal distances away from the center of an arc. Note that both distributions go to zero at the maximum arc width of ±120 km in this case.

## 3. Results

[13] We calculate the primary ionization rates for a variety of incident proton auroral conditions. Ionization results presented here are generated by the direct impact of protons and hydrogen atoms in charge exchange and ionization collisions. The ionization by the secondary electrons, which is neglected here, can be roughly estimated by multiplying primary ionization rates by 0.006 $E_0$, as suggested by *Lilensten and Galand* [1998]. $E_0$ is the characteristic energy of a Maxwellian proton flux in keV. For example, in the case of $E_0$ = 8 keV, the secondary electrons yield an electron production rate which is approximately 4.8% of that induced by direct proton and H atom impacts. The ionization contribution of secondary electrons drops off rapidly below the primary ionization peak altitudes.

### 3.1. Maxwellian Injection

[14] Figure 2 is a plot of ionization rates for a variety of topside precipitation conditions. All of the plots assume a homogenous latitudinal distribution (equation (1)) with a Maxwellian energy spectrum, and a magnetic field dip angle of $\gamma = 90°$ (vertical field lines). The three rows show results with different finite arc widths of $W$ = 30 km, 60 km, and 120 km, while the three columns show results with different characteristic energies of $E_0$ = 4 keV, 8 keV, and 20 keV, as indicated on each plot.

[15] The spatial spreading effect is quite clear in each of these plots. There are significant ionization and charge exchange collisions outside the dimensions of the initial arc width. The $X$-direction extent of the region with significant ionization correlates well with the $W$ values of the topside arc width. The rates within the precipitation zone are not uniform, but rather drop off as the $X$ distance approaches $\pm W$. The beam spreading effect clearly manifests itself in the latitudinal variation of resulting ionization rates,

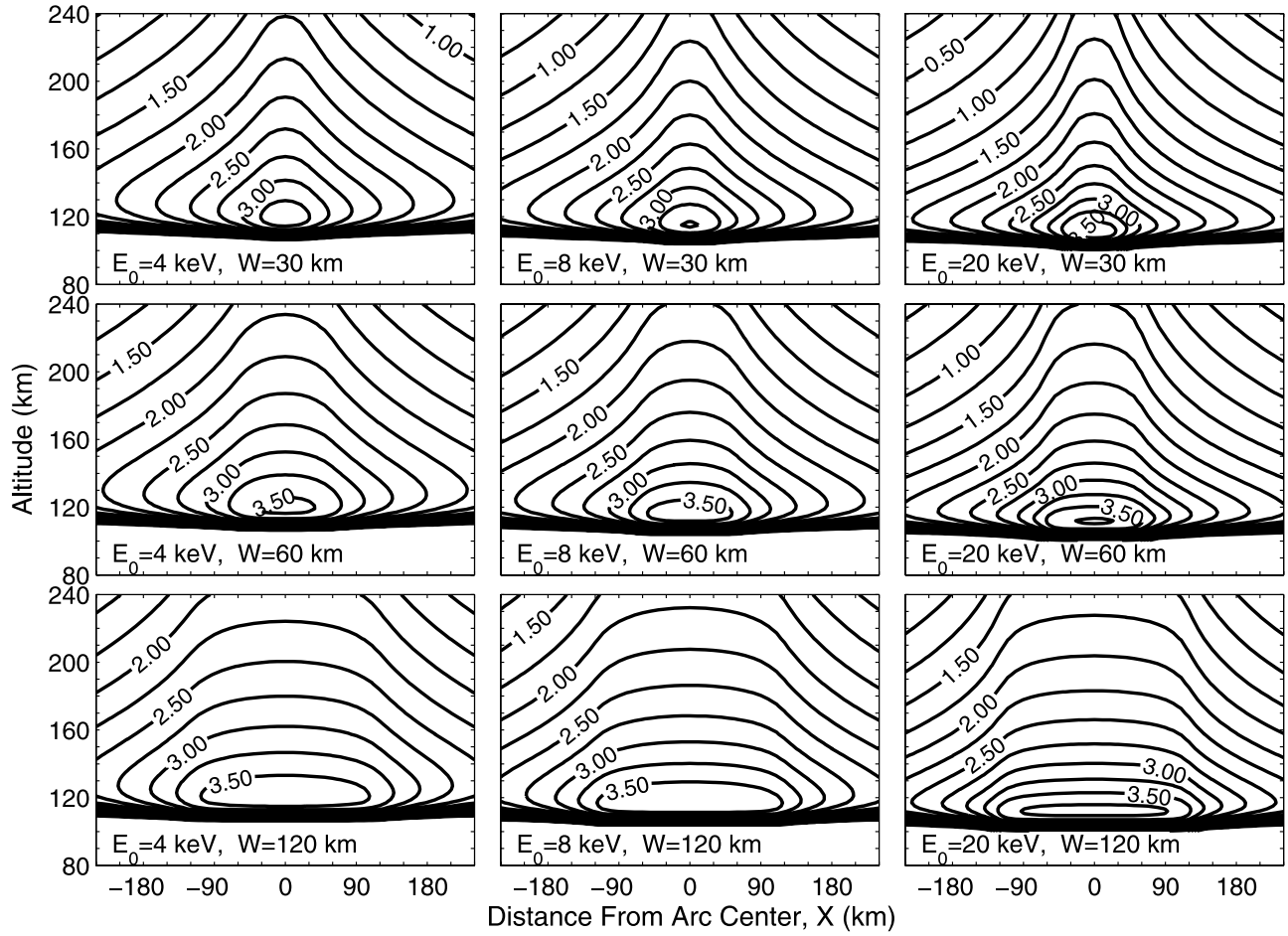


**Figure 2.** Ionization rates ($cm^{-3}$ $s^{-1}$) in the $X - Z$ plane for vertical field lines ($\gamma = 90°$) using equation (1) as the upper boundary condition with arc widths of $W = 30$, 60, and 120 km (3 rows) and Maxwellian energy spectra of $E_0 = 4$, 8, and 20 keV (3 columns). The ionization rates are shown on a logarithmic scale with contours every 0.25 decade.

in spite of the constant intensity of proton impact overhead. It is seen that higher energy precipitation leads to deeper penetration and larger ionization peak values, confirming earlier results [e.g., *Jasperse and Basu*, 1982; *Strickland et al.*, 1993; *Galand et al.*, 1999; *Fang et al.*, 2004].

[16] Figure 3 shows a comparison of results for a tilted and a vertical field line. Figure 3a presents ionization rates for a homogeneous topside boundary condition identical to that used in the lower middle panel of Figure 2 ($E_0 = 8$ keV, $W = 120$ km) except with $\gamma = 60°$. The dashed line shows the location of the field line at the center of the arc. Figure 3b overplots these ionization rates on top of those for $\gamma = 90°$, with $X$-axis values being the distance from the central field line. We know that $\gamma = 60°$ is beyond the normal dip angle range in the auroral zone. However, the study undertaken here for the the proton arc spreading effect is applicable to ring current proton precipitation as well as to auroral protons. Thus we used a relatively large inclination ($\gamma = 60°$) to illustrate the effect of the tilted magnetic field lines.

[17] Figure 3 shows that the ionization rates are nearly symmetric about the central magnetic field lines, even when the field line is tilted. The ionization rates within the precipitation zone ($|X| < 120$ km in this case) are almost identical between the two dip angles. One difference is that the peak ionization region, as illustrated by the "3.5" contour line, is larger for the $\gamma = 90°$ results than for $\gamma = 60°$. As magnetic field lines become less tilted, there is deeper penetration because there is less proton loss in each high-altitude bin (that is, the path length per $\Delta Z$ is shorter as $\gamma$ increases). The influence of the tilted magnetic field will be even less in the auroral zone, where the dip angles are typically between the selected values of 90° and 60°.

[18] It is not until far away from the central region that asymmetric characteristics appear in the tilted magnetic field case. In the positive $X$ direction, asymmetric structure is more apparent at lower altitudes (e.g., 120 km) than at higher altitudes (above 150 km). The opposite is true in the negative $X$ direction. Note that the ionization rates for the simulation with a tilted magnetic field line are larger outside of the precipitation zone than those for a vertical field line. Again, this is because of the extra path length (and therefore extra transverse spread) when the field lines are tilted rather than vertical.

[19] Figure 4 presents a comparison between simulations using a homogeneous (equation (1)) and a Gaussian (equation (2)) topside latitudinal boundary conditions. The solid contour lines in each panel show ionization rates for a

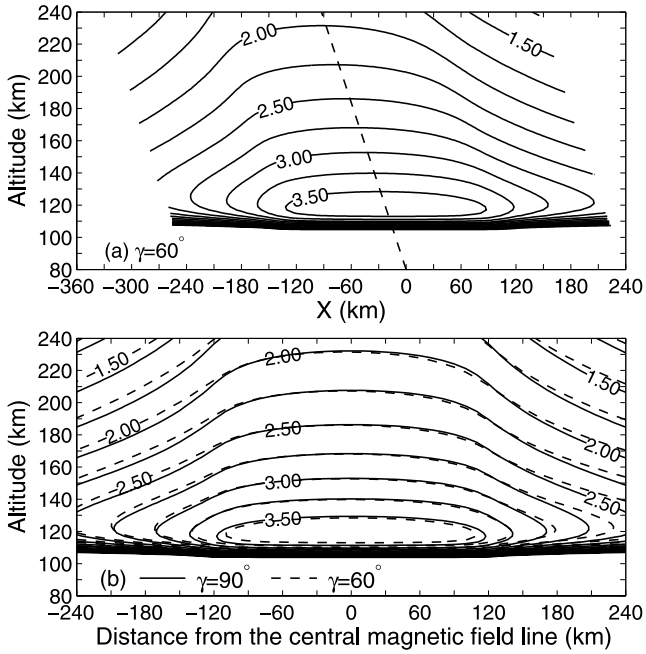


**Figure 3.** (a) Ionization rates ($cm^{-3}$ $s^{-1}$) in the $X - Z$ plane (like Figure 2) for a tilted magnetic field line ($\gamma$ = 60°), $W$ = 120 km and $E_0$ = 8 keV. (b) The values from the plot above overlaid on the corresponding plot for $\gamma$ = 90° from Figure 2, with the $X$-axis values denoting distance from the magnetic field line at the center of the arc. The results for $\gamma$ = 90° and $\gamma$ = 60° in the bottom panel are shown as solid and dashed curves, respectively.

homogeneous spatial distribution of particle energy fluxes within the incident arc width ($W$ = 120 km in these cases). The dashed contour lines are results with a Gaussian $X$-direction dependence ($FWHM$ = 240 km) of the particle flux intensity (again, within the arc width of ±120 km). Figure 4a shows results for vertical field lines while Figure 4b presents $\gamma$ = 60° simulation results.

[20] It is seen that the resulting ionization is weaker for the Gaussian upper boundary condition than for the homogeneous input, with larger differences occurring near the edges of the precipitation zone. This is anticipated since there are less incident particles correspondingly at the top (compare with Figure 1). Both sets of results show significant reductions in the ionization rates at a given altitude near the edges of the precipitation zone and substantial ionization rates outside of the proton arc. There are clearly many particles scattered outside of the original arc width.

### 3.2. Comparison to 1-D Results

[21] To quantitatively analyze the spreading effect, Figure 5 presents primary ionization rates along the central magnetic field line for a variety of simulation configurations. All of the calculations used a Maxwellian upper boundary energy spectrum with $E_0$ = 8 keV. The left-hand plots are for a homogeneous incident arc while the right-hand plots use a Gaussian $X$-dependent upper boundary condition. The top panels are for $\gamma$ = 90° and the bottom panels are for $\gamma$ = 60°. The curves in each panel are results with different arc widths (for a homogeneous distribution), or different $FWHM$ values but fixing the arc width at $W$ = 120 km (for a Gaussian distribution). With the horizontal variation neglected, 1-D results are precisely correct only for an infinite proton arc with uniform precipitation imposed overhead ($W = \infty$). Here for the sake of comparison, we present ionization rates for $W = \infty$ as well.

[22] These results emphasize the importance of the spatial spreading effect for a proton arc with finite width. Different intensities at the arc center are generated corresponding to an incident proton arc with different dimensions and different energy flux distributions. Note that the precipitation intensity at the arc center is fixed to $Q_0$ = 1 erg $cm^{-2}$ $s^{-1}$ for this comparison study. Without the lateral spreading, resulting ionization rates should have been the same along the central magnetic field line regardless of incident proton arc dimensions. However, this is not true when horizontal spreading is taken into account. For example, because the energy flux carried by a proton arc with a Gaussian distribution of $FWHM$ = 240 km and $W$ = 120 km is less than that of a uniform arc of $W$ = 120 km with the same inclination of magnetic field (dashed lines in each panel), the resulting ionization rates at the center for the Gaussian distribution are correspondingly smaller than those for the homogeneous input. This was already seen in Figure 4. On the other hand, the close agreement between a uniform arc with $W$ = 30 km and a Gaussian arc with $W$ = 120 km and $FWHM$ = 60 km (dotted lines in each panel) strongly demonstrates the particle scattering effect. That is, these latitudinal arc extents are thin relative to the transverse spreading scale, and the topside $X$ distributions are washed out by the scatter. Also, as already shown in Figure 3b, a

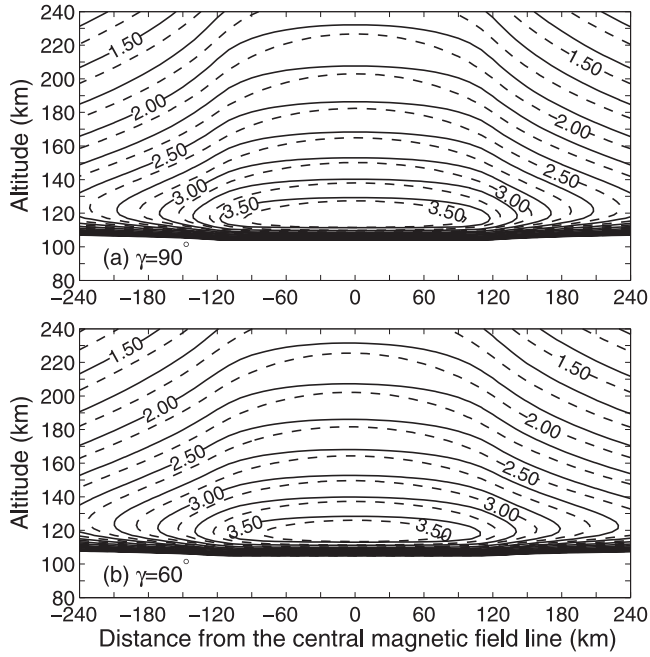


**Figure 4.** Comparison of the ionization rates ($cm^{-3}$ $s^{-1}$) between topside boundary conditions that are homogeneous (solid curves) and Gaussian (dashed curves) for a magnetic field line that is (a) vertical ($\gamma$ = 90°) and (b) tilted ($\gamma$ = 60°), with $X$-axis distance measured from the central magnetic field line. For all cases, $E_0$ = 8 keV and $W$ = 120 km (or $FWHM$ = 240 km).

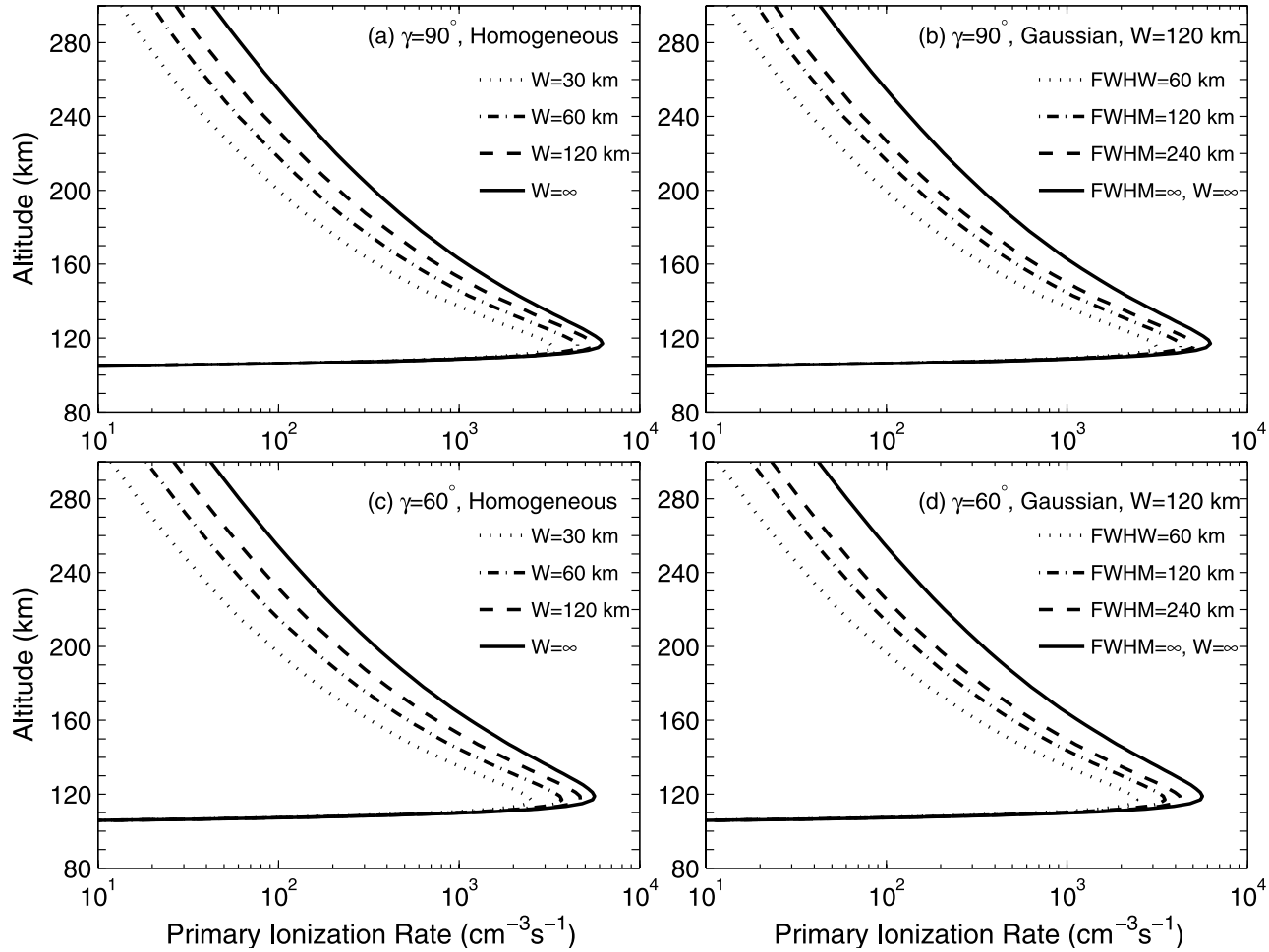


**Figure 5.** Primary ionization rates along the central magnetic field line for $E_0$ = 8 keV for (a) $\gamma = 90°$ with a homogenous boundary condition (BC), (b) $\gamma = 90°$ with a Gaussian BC, (c) $\gamma = 60°$ with a homogeneous BC, and (d) $\gamma = 60°$ with a Gaussian BC. The various lines show the results for different arc dimensions.

larger magnetic field dip angle (towards vertical) causes deeper penetration and larger ionization peaks.

[23] In 1-D models, the correction from the beam spreading effect for the case of a finite width is approximated by applying an attenuation coefficient $\varepsilon$ at the arc center. The correction factor is acquired by calculating the ratio of the total proton-hydrogen fluxes at the equilibrium altitude ($\sim$300 km) to the injection. To examine the energy dependence of the spreading effect and also for the sake of comparison to 1-D results, Table 1 presents particle flux ($H^+$ plus H) ratios between the total number flux at 300 km to that at the top along the central magnetic field line. The topside energy spectrum is Maxwellian, and results for three characteristic energies are presented: 4 keV, 8 keV, and 20 keV. Results are also given for magnetic dip angles of $\gamma = 90°$ and 60°. All of the simulations are for $W$ = 120 km (or $FWHM$ = 240 km). It is seen that $\varepsilon$ values increase with increasing characteristic energy. This is anticipated since the beam spreading is weaker with higher precipitating energy, as shown by *Kozelov* [1993] and *Fang et al.* [2004]. Correspondingly there is less attenuation above 300 km for a more energetic proton arc. In addition, $\varepsilon$ values increase with increasing magnetic dip angle and are larger for a homogeneous latitudinal distribution compared to a Gaussian distribution.

[24] It is useful to quantify the decrease in the ionization rate due to the spatial spreading effect for an incident

**Table 1.** Attenuation Coefficients of Particle Fluxes ($H^+$ Plus H) at 300 km Altitude for an Incident Proton Arc With a Maxwellian Energy Spectrum

| $E_0$, keV | Homogeneous[a] | Gaussian[b] |
|---|---|---|
| | $\gamma = 90°$ | |
| 4 | 0.75 | 0.67 |
| 8 | 0.79 | 0.71 |
| 20 | 0.86 | 0.80 |
| | $\gamma = 60°$ | |
| 4 | 0.65 | 0.57 |
| 8 | 0.69 | 0.61 |
| 20 | 0.75 | 0.68 |

[a]For a homogeneous latitudinal energy flux distribution at the top, $W$ = 120 km.

[b]For a Gaussian latitudinal energy flux distribution at the top, $W$ = 120 km, $FWHM$ = 240 km.

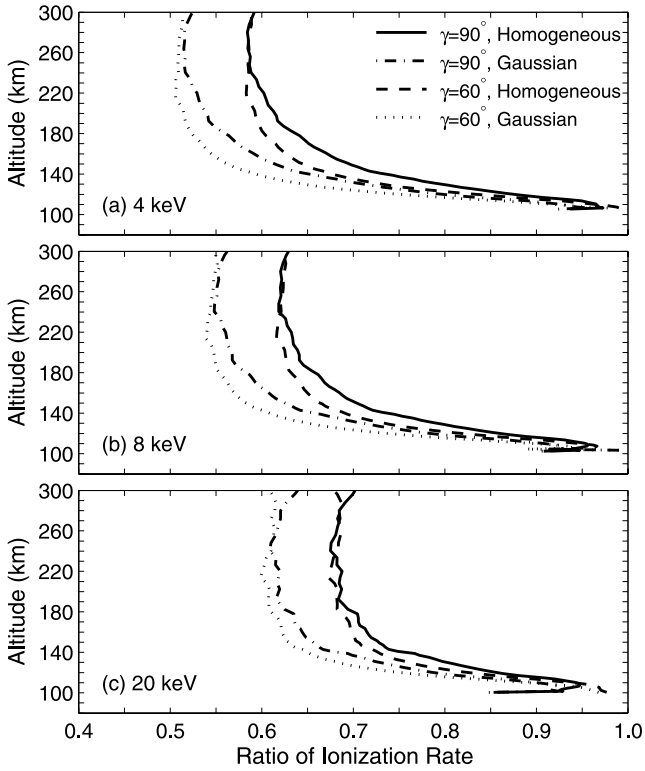


**Figure 6.** Ratio of ionization rates along the central magnetic field line between the $W$ = 120 km (or $FWHM$ = 240 km) results and the $W = \infty$ results for (a) $E_0$ = 4 keV, (b) $E_0$ = 8 keV, and (c) $E_0$ = 20 keV. The various lines are for the different tilt angles and upper BC conditions.

proton arc with finite width by comparing it with the rate for a $W = \infty$ arc. Figure 6 shows the ratio of the $W$ = 120 km (or $FWHM$ = 240 km for a Gaussian topside condition) ionization rates along the central magnetic field line to the rates for $W = \infty$. The three panels show results for $E_0$ = 4, 8, and 20 keV, respectively, and the 4 curves show the results for homogeneous and Gaussian latitudinal distributions with $\gamma = 90°$ and 60°.

[25] The percentage difference of ionization rates produced by a proton arc with limited latitudinal extent illustrates well the influence of the horizontal spatial spreading. As to the correction approximated by 1-D models, an attenuation coefficient $\varepsilon$ over an equilibrium altitude leads to an altitude-independent ratio of ionization rates below. That is, a constant ionization rate ratio of $\varepsilon$ is applied below ~300 km as a coarse correction to the beam spreading effect for 1-D calculations. However, as seen in Figure 6, the ratio of ionization rate varies significantly with altitude. For example, for a Maxwellian with a characteristic energy of $E_0$ = 8 keV, homogeneous topside input ($W$ = 120 km) in a vertical magnetic field case, the ratio of ionization rate is nearly invariant with altitude above ~240 km. Below this level, the ratio rapidly increases. Note that the transition level is located lower as incident energy increases. The altitude dependence of the ionization rate ratios indicates that the approximation of applying a correction factor $\varepsilon$ is not precisely correct for 1-D theoretical models. In the above example, $\varepsilon$ = 0.79 (see Table 1). However, our 3-D simulations show that the ionization rate ratio is around 0.62 above 240 km, but approaches 0.96 at around 108 km, as shown in Figure 6b. An assumption of an altitude independent attenuation coefficient of 0.79 in 1-D models will therefore overestimate the ionization at high altitudes (~27% in this case) and underestimate the ionization at lower altitudes (up to ~18% in this case).

[26] An interesting result seen in Figure 6 is that the attenuation profiles of primary ionization rates are very similar for the vertical and tilted magnetic field simulations (given the same topside input conditions). The vertical field line ratios begin to increase at a slightly higher altitude than the tilted field line values. There is a systematic negative offset (up to around −0.1 at low altitudes) for the tilted field line values compared to the vertical field numbers. Because of less energy flux impact for a Gaussian energy flux distribution than for a homogeneous input, it is seen that the ratios are correspondingly smaller. In addition, the change of the ionization rate ratios between high and low altitudes decreases with increasing incident energy. In other words, the error of 1-D approximation generally becomes more serious below 300 km for lower energy proton injection.

[27] Table 2 summarizes the ionization rate ratios specified at ionization peak altitudes for the calculations presented in Figure 6. By ionization peak altitude, we mean the altitude where ionization rates without the beam spreading ($W = \infty$) have a maximum. The errors between 1-D and 3-D results are also estimated at ionization peak altitudes, if the attenuation coefficients listed in Table 1 are used for the correction of 1-D results. We can see that an underestimation (up to 19% in this study) at ionization peak altitudes exists for 1-D models.

**Table 2.** Ratio of Primary Ionization Rate at Ionization Peak Altitude for the Calculations Presented in Figure 6[a]

| | | | Ratio of Ionization Rate | | Error of 1-D Results, % | |
|---|---|---|---|---|---|---|
| $E_0$, keV | γ, deg | Peak Altitude, km | Homogeneous[b] | Gaussian[c] | Homogeneous | Gaussian |
| 4 | 90 | 121 | 0.87 | 0.79 | −13.8 | −15.2 |
| 4 | 60 | 125 | 0.77 | 0.69 | −15.6 | −17.4 |
| 8 | 90 | 117 | 0.89 | 0.82 | −11.2 | −13.4 |
| 8 | 60 | 119 | 0.83 | 0.75 | −16.9 | −18.7 |
| 20 | 90 | 112 | 0.93 | 0.88 | −7.5 | −9.1 |
| 20 | 60 | 114 | 0.90 | 0.84 | −16.7 | −19.0 |

[a]The incident proton arc has a Maxwellian energy spectrum.
[b]For a homogeneous latitudinal energy flux distribution at the top, $W$ = 120 km.
[c]For a Gaussian distribution at the top, $W$ = 120 km, $FWHM$ = 240 km.

**Table 3.** Attenuation Coefficients[a]

| *E*, keV | Homogeneous | Gaussian |
|---|---|---|
| | $\gamma = 90°$ | |
| 4 | 0.72 | 0.64 |
| 8 | 0.76 | 0.68 |
| 20 | 0.81 | 0.74 |
| | $\gamma = 60°$ | |
| 4 | 0.62 | 0.55 |
| 8 | 0.66 | 0.59 |
| 20 | 0.72 | 0.64 |

[a]Similar to Table 1, but for an incident monoenergetic proton arc.

[28] Note that at higher altitudes, the ionization rate ratio presented in Figure 6 increases again (not shown). Above ~400 km, the ratio begins to rise and reaches unity somewhere above ~500 km (the precise altitudes depend on input characteristic energy and arc width). This is because of fewer particle scattering collisions at higher altitudes.

### 3.3. Monoenergetic Injection

[29] In subsection 3.1, we extensively examined the influence of a variety of incident proton arc conditions on the resulting ionization rates when the spatial spreading effect was taken into account. A comparison of 1-D approximations and 3-D results below an equilibrium altitude was made in subsection 3.2. We have seen that the correction using an attenuation coefficient $\varepsilon$ to 1-D calculations is not accurate enough. In general, ionization rates are overestimated at high altitudes but underestimated at low altitudes. The influence of an incident average energy is well demonstrated on the attenuation of particle fluxes and resulting ionization rates. In the above discussion, the proton precipitation has a Maxwellian energy distribution. However, some questions still remain unresolved. Can the altitude dependence of the ionization rate ratio be attributed to the incident energy distribution? Does the correction using an attenuation coefficient $\varepsilon$ in 1-D models work fine with a monoenergetic proton arc? To answer these questions, we examine in this subsection the spatial spreading effect for a monoenergetic proton arc at the top of the atmosphere.

[30] Similar to Table 1, we present in Table 3 the attenuation coefficients of particle fluxes ($H^+$ plus H) at 300 km altitude but for an incident monoenergetic proton arc. A similar trend with varying parameters is also demonstrated. It is worth noting that $\varepsilon$ values for a monoenergetic injection are systematically smaller than those for a Maxwellian input with the same characteristic energy. The results presented in Tables 1 and 3 are consistent with each other, when one considers that in a Maxwellian distribution the average particle energy is two times larger than the characteristic energy.

[31] Figure 7 shows ionization rates along the central magnetic field line for a variety of topside precipitating conditions similar to Figure 5 but for a monoenergetic injection of 8 keV. Again, the spatial spreading effect is strongly demonstrated in the comparison among different proton arc dimensions. Of particular interest in Figure 7 is that even for a monoenergetic incident arc at the topside boundary, there is still an altitude dependence for the ratios of ionization rates between limited $W$ or $FWHM$ values to $W = \infty$ ($FWHM = \infty$).

[32] To quantitatively analyze the percentage difference due to the beam spreading, we present in Figure 8a the ionization rate along the central magnetic field line ($\gamma = 90°$) for a homogeneous distribution with latitudinal semiwidth of $W = 120$ km and $W = \infty$. The results are shown for an incident Maxwellian energy spectrum of $E_0 = 8$ keV and for a monoenergetic input of 16 keV. The precipitating particles have the same average energy of 16 keV in the two distributions. The ratios of the $W = 120$ km ionization rates to the rates for $W = \infty$ are displayed in Figure 8b for the two incident energy spectra. The effective beam radii of the ionization rates for fine proton beams, which are incident at one point on the topside boundary, are also shown in Figure 8b. An effective beam radius for an incident fine beam is defined as the distance away from the center, within which 80% of quantities are confined [*Kozelov*, 1993; *Fang et al.*, 2004]. As seen in Figure 8, an altitude dependence of the ionization rate ratio also exists for a monoenergeitc incident arc. The approximation of applying a correction factor $\varepsilon$ in 1-D models, therefore, still introduces a significant error even for a monoenergetic injection. Although the ionization rates for the Maxwellian and for the single energy input are notably separated (Figure 8a), we find that the altitude variation of the ionization rate ratios as well as the effective beam radii is almost identical for the two incident energy spectra except at very low altitude (Figure 8b). It is implied that incident energy distributions are not a determinant factor in the altitude-dependent attenuation of ionization rates for a proton arc with finite width.

## 4. Discussion

[33] We have shown that the ratio of the ionization rate along the central magnetic field line for the case of an incident proton arc with finite width to the ionization rate for $W = \infty$ increases as altitude decreases. The altitude-varying attenuation of the ionization rates can not be represented by an invariant correction factor $\varepsilon < 1$ over the whole altitude range below ~300 km in 1-D models. As a result, ionization rates are generally overestimated at high altitudes and underestimated at low altitudes by 1-D models, if applying $\varepsilon$ as an approximation of the correction to the beam spreading effect. The comparison between a Maxwellian and a monoenergetic particle injection with a same average energy in Figure 8 implies that precipitating energy distributions can not account for the altitude dependence of ionization rate ratios. We still need to explore the physics hidden behind these results.

### 4.1. Proton/Hydrogen Fraction Ratio

[34] Recognizing that protons and hydrogen atoms are mixed at an equilibrium altitude around 300 km due to charge exchange/electron stripping collisions, we will examine the possibility of the charge fraction ratio acting as a driving force in the altitude-dependent attenuation of the ionization rate. As for the correction usually conducted in 1-D models, an attenuation coefficient $\varepsilon$ can be evaluated by calculating the ratio of total $H^+$ and H fluxes at ~300 km altitude to the incident proton intensity. In the $\varepsilon$ calculation, the proton/hydrogen fraction ratio at ~300 km

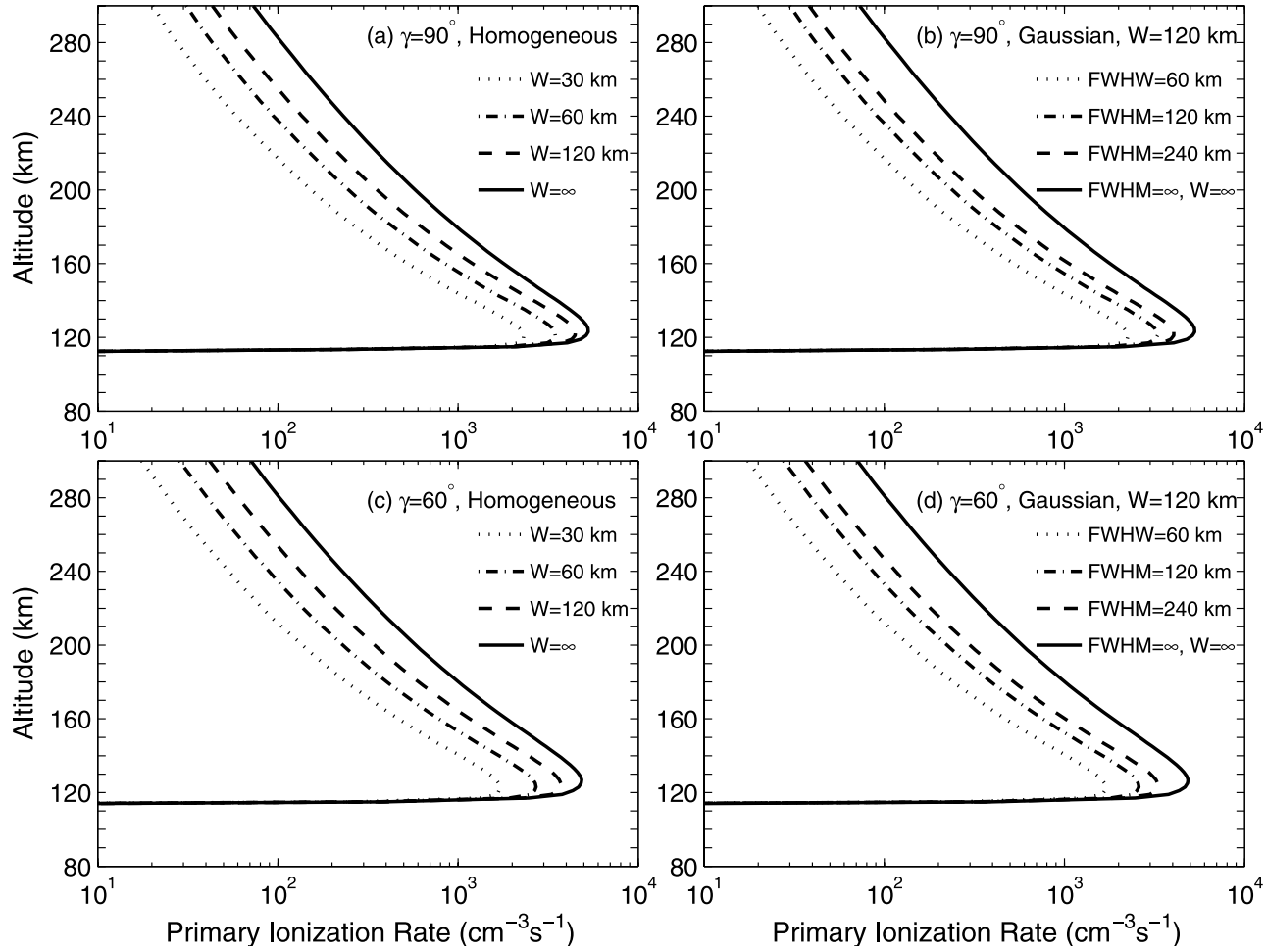


**Figure 7.** Similar to Figure 5 but for a monoenergetic proton injection of E = 8 keV.

altitude is neglected. One question arises: can a more accurate correction to 1-D results produce the altitude-varying ratios of the ionization rates, when the difference of the particle transport below ~300 km is taken into account between protons and hydrogen atoms? To better focus on the possible role of the $H^+$/H fraction ratio, the beam spreading is excluded here, just as what 1-D models do.

[35] Let us denote the attenuation coefficients of protons and hydrogen atoms by $\varepsilon_P$ and $\varepsilon_H$, respectively. That is, $\varepsilon_P = \Phi_P/\Phi_\infty$, $\varepsilon_H = \Phi_H/\Phi_\infty$, where $\Phi_P$, $\Phi_H$ are the proton and hydrogen atom fluxes at an equilibrium altitude, and $\Phi_\infty$ is the incident proton flux at 950 km. We have

$$\varepsilon = (\Phi_P + \Phi_H)/\Phi_\infty = \varepsilon_P + \varepsilon_H. \tag{3}$$

The ionization rate below ~300 km is given by

$$\eta(z) = \varepsilon_P \eta_p(z) + \varepsilon_H \eta_H(z), \tag{4}$$

where $z < 300$ km along the central magnetic field line, $\eta_p(z)$ and $\eta_H(z)$ are the ionization rates generated by precipitating pure protons and pure hydrogen atoms at 300 km altitude, respectively. To calculate $\eta_p(z)$ and $\eta_H(z)$, ionization rates are scaled to an incident energy flux of 1 erg $cm^{-2}$ $s^{-1}$. Keep in mind that the energy loss above ~300 km is omitted in 1-D calculations. Therefore, a more accurate correction is written as

$$\varepsilon^*(z) = \frac{\eta(z)}{\eta_\infty(z)} = \frac{\varepsilon_P \eta_p(z) + \varepsilon_H \eta_H(z)}{\eta_\infty(z)}, \tag{5}$$

where $\eta_\infty(z)$ is the ionization rate for pure topside (950 km) $H^+$ precipitation with a normalized energy flux.

[36] To analyze how $\varepsilon^*$ varies with altitude, we need to evaluate $\eta_p(z)$, $\eta_H(z)$, and $\eta_\infty(z)$ separately. Figure 9 presents the ionization rates for four types of particle injection: pure $H^+$ and pure H atom precipitation at 950 km altitude and at 300 km altitude. All of the other conditions are kept the same. The incident particles have a Maxwellian energy distribution of $E_0$ = 8 keV. The magnetic field lines are vertical, $\gamma = 90°$. In this comparison, the beam spreading effect has been turned off. As shown in Figure 9, the ionization rates for the different topside boundary conditions are essentially identical below 300 km. The pure $H^+$ injection at 950 km altitude generates a little higher ionization production above 400 km than that for the pure H atom precipitation. Below ~400 km, repeated charge exchange/electron stripping collisions in a much denser atmosphere make the charge state frequently change between $H^+$ and H. As a result, the difference due to

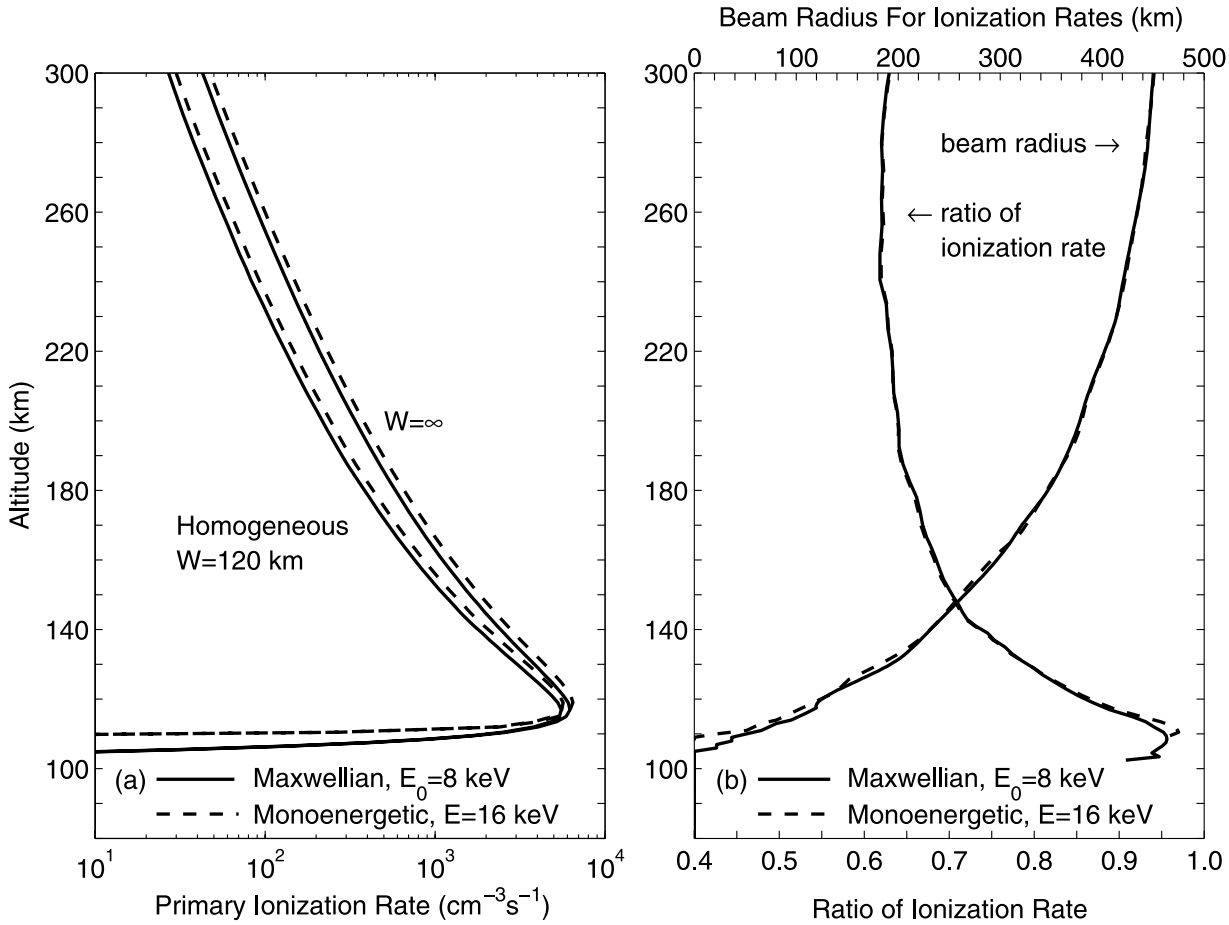


**Figure 8.** (a) Primary ionization rate along the central magnetic field line ($\gamma = 90°$) with the beam spreading effect considered or neglected, as indicated near the curves. (b) Ratio of ionization rates between the results for $W = 120$ km and $W = \infty$. The effective beam radii in association with ionization rate are also displayed for a fine proton beam incident at one point. The calculations are made for a precipitating Maxwellian spectrum of $E_0 = 8$ keV (solid curves) and a monoenergetic injection of 16 keV (dashed curves).

incident protons and hydrogen atoms disappears at low altitudes, considering that the energy loss at high altitudes is negligible compared to the peak energy deposition [e.g., *Basu et al.*, 2001; *Fang et al.*, 2004]. For the proton and hydrogen atom injection at a lower topside boundary of 300 km, the ionizations rapidly merge with the two other curves for the precipitation at 950 km altitude.

[37] As illustrated in Figure 9, the equality of $\eta_p(z) = \eta_H(z) = \eta_\infty(z)$ is satisfied very well below ~280 km altitude. Equation (5) can thus be reduced to

$$\varepsilon^*(z) = \varepsilon_P + \varepsilon_H = \varepsilon. \tag{6}$$

We can see that the consideration of the $H^+/H$ fraction ratio at an equilibrium altitude does not help explain the results. That is, the altitude-dependent attenuation of the ionization rate below ~300 km cannot be explained in 1-D context.

### 4.2. Beam Spreading Effect

[38] We have just shown that 1-D methods fail in explaining the altitude-varying ionization rate ratios along a central magnetic field line between a proton arc with finite width and a $W = \infty$ arc. It prompts us to invoke the beam spreading effect to rethink the problem from a 3-D perspective.

[39] For the case of an incident proton arc with finite width, the ionization rate along a central magnetic field line at $Z$ altitude is evaluated by integrating all of the ionization contribution from the topside injection over the whole arc. To simplify our discussion and notation we assume, without loss of generality, the incident proton arc has a circular shape with a radius of $R$. In addition, there is a uniform energy flux distribution at the topside boundary, $Q_0 = 1$ erg cm$^{-2}$ s$^{-1}$. The magnetic field lines are vertical. In this case, the ionization rate can be equivalently assessed in another way, if replacing the proton arc with a fine beam incident at the topside boundary. By the fine beam, we mean the beam cross section is 1 cm$^2$. Particles are precipitating at the center with a normalized energy flux, and there is no particle injection elsewhere. By this means, the ionization rate can be equivalently obtained by counting the number of ionization events occurring in an altitude interval of 1 cm at $Z$ altitude and within a radius of $R$ from the center. As $R$ approaches $\infty$ in the ionization integration, the ionization rate at $Z$ altitude for an

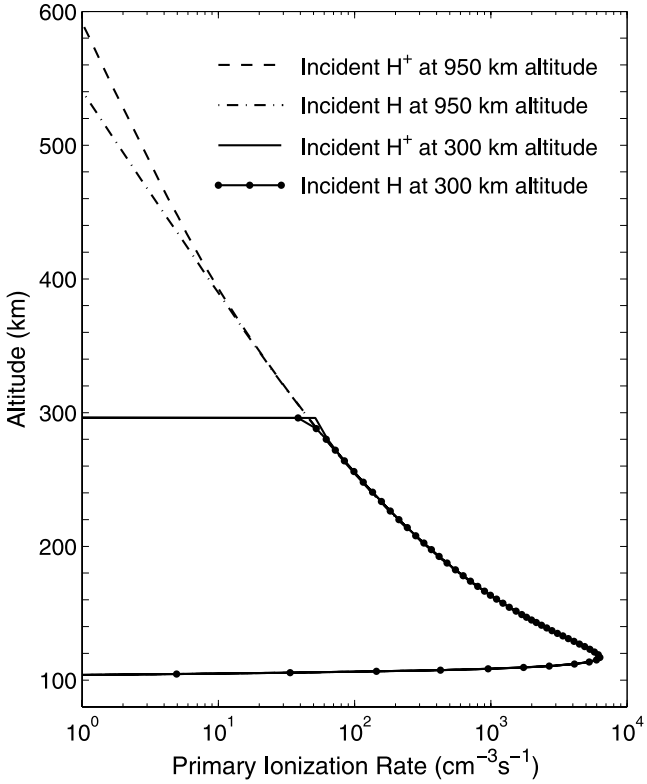


**Figure 9.** Primary ionization rate versus altitude for 4 types of particle injection: pure proton and pure hydrogen atom precipitation at 950 km altitude and at 300 km altitude. All incident particle energy spectra are isotropic Maxwellian distributions with $E_0$ = 8 keV. The magnetic field lines are vertical, $\gamma = 90°$. The beam spreading effect is neglected.

infinite proton arc can be approached as well. In other words, an ionization rate ratio between a proton arc with finite width and a $R = \infty$ arc, in which we are actually interested, can be equivalently evaluated through the ratio of the integrated ionization within a radius of $R$ to those summed up over the whole horizontal plane for a fine beam injection. In essence, the attenuation of the ionization rates is determined by how strong an incident fine beam spreads at a given altitude. The wider the beam spreads, the more attenuation the ionization rates have.

[40] The correlation between the ionization rate ratios and the beam spreading is confirmed in Figure 8b, where we present the altitude profiles for the ionization rate ratios as well as the effective beam radii. It is seen that as altitude decreases, the effective beam radii decrease. Here, an effective beam radius is defined in association with ionization production for an incident fine beam. That is, 80% of the ionization events are confined within the beam radius. Note that the effective beam radii are not invariant with altitude. The shrink of the effective beam radii with the decrease of altitude can be interpreted, as we observe the horizontal distribution of the average velocity angles of protons and hydrogen atoms with respect to the vertical direction, as shown in Figure 6 of *Fang et al.* [2004]. While the atmospheric parameters used there are different from what we employ in this paper, it illustrates well that on average the velocity angles are increasing away from the incident magnetic field line. The angle enhancement with the distance away from the center results in more energy loss through an altitude bin because of the longer traveling path. The particles which are scattered above ~300 km altitude to the outside edge of the beam are thus liable to be terminated earlier over their penetration below ~300 km. Therefore as altitude decreases, the effective beam radius becomes smaller. As a result, the proportion of the integrated ionization production within a fixed distance of $R$ becomes higher compared to the total ionization over the whole horizontal plane. Accordingly, the ratio of the ionization rates between a proton arc with finite width and a $R = \infty$ arc increases with decreasing altitude. This trend is clearly observed in Figure 8b.

[41] An interesting feature we have already seen in Figure 8 is that the ionization rate ratios for a Maxwellian and a monoenergetic proton arcs with a same average energy input coincide with each other except at very low altitude. In the mean time, the altitude profiles of the effective beam radii have a very close agreement for the two incident energy spectra. The correlation between the ionization rate ratios and the beam radii is ensured. Moreover, the location of the transition region between slow variation at high altitudes to rapid change at low altitudes is consistent between the effective beam radii and the ionization rate ratios. This provides further support to our analysis. Through the comparison in Figure 8, as well as the discussion regarding effective beam radius made by *Fang et al.* [2004], an important conclusion we can draw is that the mean energy of the incident protons is a key factor in the horizontal spreading, and thus determines how ionization rates attenuate with altitude for a proton arc with finite width. The energy distribution with a given mean energy only has a second order effect on the beam spreading and thus ionization rate ratios, mostly at very low altitudes (Figure 8b). It was found that precipitating particles with a higher incident energy generally have weaker spatial spreading. However, below ~120 km, their effective beam radii are a bit larger than those of lower energy input since they have deeper penetration into the atmosphere [*Kozelov*, 1993; *Fang et al.*, 2004]. Because there is a high energy tail in a Maxwellian spectrum that is absent with a monoenergetic input, it is anticipated that the beam radii below ~120 km are a bit larger for the Maxwellian input. The ionization rate ratios are therefore correspondingly smaller, as shown in Figure 8b. Similarly, the energy dependence of the beam spreading can be used to explain Figure 6, where more energetic particle input has a bigger ionization rate ratio at high altitudes and a little smaller value at very low altitudes.

[42] In the comparison between the $\varepsilon$ values used by 1-D models for the beam spreading correction in the case of an incident proton arc with finite width (Tables 1 and 3) and the ionization rate ratios accurately calculated by our 3-D Monte Carlo model (Figures 6 and 8), it is found that the $\varepsilon$ values are generally larger than the ionization rate ratios above ~150 km and smaller at altitudes below. From a view of ionization rates, a simplified altitude-independent correction factor $\varepsilon$ underestimates the beam spreading at high altitudes and overestimates it at low altitudes. Note that $\varepsilon$ is calculated based on the relative intensity of particle fluxes to the topside input (equation (3)). That is, the attenuation of

the ionization rates is approximated by considering the beam spreading of particle fluxes in 1-D models. However, *Fang et al.* [2004] showed that the beam spreading effect was different for the particle fluxes and for the ionization rates. The effective beam radii for the ionization rates are more than two times larger than those for the particle fluxes ($H^+$ plus H), because on average the particle velocity angles with respect to the vertical direction are increasing away from the beam center. As a result, an overestimation of the ionization rate is inevitable at high altitudes by using $\varepsilon$ in 1-D models, since the beam spreading for the ionization rates is underestimated by overlooking the difference of the spatial spreading between the particle fluxes and the ionization rates. As the effective beam radius approaches zero at low altitudes, an underestimation of the ionization rates is caused by 1-D models, because of the overestimation of the beam spreading using the estimation derived at the equilibrium altitude.

[43] As illustrated in Figure 3 and Tables 1 and 3, particle precipitation in the case of a tilted magnetic field has a stronger spreading effect than in a vertical field. This is the reason why in Figure 6 the ratios of ionization rates for a tilted magnetic field are systematically less than those for a vertical field case.

[44] The nonuniformity of the magnetic field and the anisotropy of incident pitch angles, which are neglected in our current model, can affect the altitude-varying attenuation of the ionization rates through spatial spreading. The convergence of the geomagnetic field in the auroral region can weaken the spreading effect and thus increase the ionization rate ratios. The anisotropic pitch angle distribution likewise comes into play. An incident pitch angle distribution peak in the direction parallel to the magnetic field lines can decrease the effective beam radii and increase the ratios of the ionization rates. The result is opposite for a pitch angle distribution peak in the perpendicular direction to the magnetic field lines.

## 5. Summary and Conclusion

[45] The influence of latitudinal spreading of a proton arc on the resulting primary ionization rate has been extensively investigated. Our three-dimensional Monte Carlo ion transport model [*Fang et al.*, 2004] was used to quantify this effect for a variety of simulation set-up configurations. Two-dimensional results in the $X - Z$ plane were presented to show the latitudinal extent of the spreading in the ionization rates. The particle fluxes and ionization rates were then examined along the central magnetic field line of a proton precipitation band (infinite longitudinal extend but finite latitudinal extent) to understand the relationship of these results to 1-D model calculations. Results were compared against those from an arc of infinite spatial extent (that is, a simulation with no spreading influence) to show how the resulting ionization rates vary with altitude when the transverse beam spreading effect is taken into account. Several characteristic energies were examined, along with a variety of arc widths, topside spatial energy flux distributions, and magnetic field line dip angles.

[46] The 2-D ionization rate plots showed that the ionization rates are not confined only to the latitudinal extent of the precipitation zone. There is significant reduction of the ionization rates at a given altitude near the edge of the precipitation zone. This smoothly transitions into substantial ionization rates beyond the precipitation edges, particularly below 150 km. The results with tilted field lines showed that the ionization pattern is nearly symmetric about the incident magnetic field line except far away from the central region. Similar results were observed by *Davidson* [1965] in the analysis of an incident fine proton beam with tilted magnetic field lines. As shown in Figure 3 and Figure 4, asymmetry is most apparent beyond the precipitation zone, but it is not large.

[47] From the central field line comparisons, it was found that the spreading effect of a proton arc depends on all of the parameters that were investigated: characteristic energy, arc width, homogeneous or Gaussian energy flux distribution in the latitudinal direction, and the inclination of the magnetic field lines. Even for a proton arc with a semiwidth of $W$ = 120 km, the spatial spreading effect still cannot be neglected.

[48] An important result is that the ionization rate ratios for an incident proton arc with limited latitudinal extent compared to those for a $W = \infty$ arc increase along the central magnetic field line as altitude decreases. The altitude-varying attenuation of the ionization rates implies that a single correction factor $\varepsilon < 1$, often introduced in 1-D models at the center of a proton arc with finite width, can not completely account for the spreading effect. In 1-D models, the correction factor $\varepsilon$, which is derived at an equilibrium altitude ($\sim$300 km), is applied to all of the ionization rates for $W = \infty$ below $\sim$300 km. That is, an altitude-independent ratio ($\varepsilon$) of the ionization rate is approximated as the correction to the spreading effect in 1-D models. As a result, ionization rates along the central magnetic field line are generally overestimated by 1-D models at high altitudes (above $\sim$150 km) and underestimated at low altitudes (below $\sim$150 km).

[49] The altitude dependence of the ionization rate ratios exists even for monoenergetic proton precipitation at the top. Although the ionization rates are notably separated for a Maxwellian energy spectrum and for a monoenergetic energy input with a same average energy, the altitude profiles of the ionization rate ratios coincide with each other for the two energy injection, except at very low altitudes. This agreement suggests that the energy distribution of the precipitating particles is not a determinant factor in the altitude variation of the ionization rate ratios. The mean energy of the incident protons is what matters.

[50] It is found that the proton/hydrogen fraction ratio at the equilibrium altitude can not explain the altitude-varying ionization rate ratios in 1-D context, either. The resulting ionization rates below $\sim$300 km essentially are the same regardless of the charge state of the precipitating particles, because of the frequent charge exchange/electron stripping collisions. Therefore, the correction factor is still altitude independent in 1-D models, even after the consideration of the charge state mixing ratio at $\sim$300 km altitude.

[51] Our investigation shows that the spreading effect for a proton arc with finite width is the critical reason responsible for the altitude-varying attenuation of the ionization rates. In essence, the attenuation of the ionization rates is determined by how strong an incident beam spreads at a given altitude. The wider the energetic

particles spread, the more attenuation the ionization rates have.

[52] The average velocity angles of protons and hydrogen atoms with respect to the vertical direction are increasing away from the central magnetic field line for an incident fine beam [*Fang et al.*, 2004]. Accordingly, the particles scattered to the outside edge of the beam above ~300 km altitude are more likely to be thermalized at higher altitudes, because they undergo more energy loss per altitude bin. As a result, the effective beam radius shrinks with decreasing altitude. The ratios of the ionization rates between a proton arc with finite width and a $W = \infty$ arc are thus increasing. As the effective beam radius approaches zero at low altitudes, an underestimation of the ionization rates is caused by 1-D models, because of the overestimation of the beam spreading using the value derived at the equilibrium altitude.

[53] The overestimation of the ionization rates at high altitudes in 1-D models comes from the neglect of the difference of the spreading effect between the particle fluxes and the ionization rates. As shown by *Fang et al.* [2004], the effective beam radii for the ionization rates are more than two times larger than those for the particle fluxes. However, the correction factor $\varepsilon$ is calculated based on the relative intensity of the particle fluxes at ~300 km altitude to the topside injection. Therefore, an underestimation of the beam spreading is inevitable. This is responsible for the overestimation of the ionization rates above ~150 km altitude.

[54] The question still arises of how to apply the results of this study to 1-D proton precipitation models. Two possibilities are evident. The first is to apply one of the ionization rate ratios presented above, whichever one most closely matches the conditions of interest. Another option is to use an $\varepsilon$ value that will yield the correct ionization rate reduction for a specific altitude of interest (for example, at the ionization peak). A parameterized formula for the altitude-varying ionization rate ratio will be the goal of a future study.

[55] **Acknowledgments.** We would like to thank Marina Galand for her enriching comments. Our special thanks are due to James Sharber for supplying the authors with a reprint of his paper and helpful discussions. This work was supported by NASA grants NAG 5-5030 and NAG 5-11831, and NSF grant ATM-0090165.

[56] Shadia Rifai Habbal thanks Marina Galand and Dag Lorentzen for their assistance in evaluating this paper.

## References

Basu, B., J. R. Jasperse, R. M. Robinson, R. R. Vondrak, and D. S. Evans (1987), Linear transport theory of auroral proton precipitation: A comparison with observations, *J. Geophys. Res.*, *92*, 5920.

Basu, B., J. R. Jasperse, D. J. Strickland, and R. E. Daniell Jr. (1993), Transport-theoretic model for the electron-proton-hydrogen atom aurora: 1. Theory, *J. Geophys. Res.*, *98*, 21,517.

Basu, B., D. T. Decker, and J. R. Jasperse (2001), Proton transport model: A review, *J. Geophys. Res.*, *106*, 93.

Davidson, G. T. (1965), Expected spatial distribution of low energy protons precipitated in the auroral zones, *J. Geophys. Res.*, *70*, 1061.

Decker, D. T., B. V. Kozelov, B. Basu, J. R. Jasperse, and V. E. Ivanov (1996), Collisional degradation of the proton-H atom fluxes in the atmosphere: A comparison of theoretical techniques, *J. Geophys. Res.*, *101*, 26,947.

Fang, X., M. W. Liemohn, J. U. Kozyra, and S. C. Solomon (2004), Quantification of the spreading effect of auroral proton precipitation, *J. Geophys. Res.*, *109*, A04309, doi:10.1029/2003JA010119.

Galand, M., and A. D. Richmond (2001), Ionospheric electrical conductances produced by auroral proton precipitation, *J. Geophys. Res.*, *106*, 117.

Galand, M., J. Lilensten, W. Kofman, and R. B. Sidge (1997), Proton transport model in the ionosphere: 1. Multistream approach of the transport equations, *J. Geophys. Res.*, *102*, 22,261.

Galand, M., R. G. Roble, and D. Lummerzheim (1999), Ionization by energetic protons in Thermosphere-Ionosphere Electrodynamics General Circulation Model, *J. Geophys. Res.*, *104*, 27,973.

Galand, M., T. J. Fuller-Rowell, and M. V. Codrescu (2001), Response of the upper atmosphere to auroral protons, *J. Geophys. Res.*, *106*, 127.

Gussenhoven, M. S., D. A. Hardy, and N. Heinemann (1987), The equatorward boundary of auroral ion precipitation, *J. Geophys. Res.*, *92*, 3273.

Hardy, D. A., M. S. Gussenhoven, and D. Brautigam (1989), A statistical model of auroral ion precipitation, *J. Geophys. Res.*, *94*, 370.

Hedin, A. E. (1991), Extension of the MSIS thermosphere model into the middle and lower atmosphere, *J. Geophys. Res.*, *96*, 1159.

Igelesias, G. E., and R. R. Vondrak (1974), Atmospheric spreading of protons in auroral arcs, *J. Geophys. Res.*, *79*, 280.

Jasperse, J. R., and B. Basu (1982), Transport-theoretic solutions for auroral proton and H atom fluxes and related quantities, *J. Geophys. Res.*, *87*, 811.

Johnstone, A. D. (1972), The spreading of a proton beam by the atmosphere, *Planet. Space Sci.*, *20*, 292.

Kallio, E., and S. Barabash (2001), Atmospheric effects of precipitating energetic hydrogen atoms on the Martian atmosphere, *J. Geophys. Res.*, *106*, 165.

Kozelov, B. V. (1993), Influence of the dipolar magnetic field on transport of proton-H atom fluxes in the atmosphere, *Ann. Geophys.*, *11*, 697.

Kozelov, B. V., and V. E. Ivanov (1992), Monte Carlo calculations of proton-hydrogen atom transport in N2, *Planet. Space Sci.*, *40*, 1503.

Lilensten, J., and M. Galand (1998), Proton-electron precipitation effects on the electron production and density above EISCAT (Tromsø) and ESR, *Ann. Geophys.*, *16*, 1299.

Lorentzen, D. A. (2000), Latitudinal and longitudinal dispersion of energetic auroral protons, *Ann. Geophys.*, *18*, 81.

McNeal, R. J., and J. H. Birely (1973), Laboratory studies of collisions of energetic $H^+$ and hydrogen with atmospheric constituents, *Rev. Geophys.*, *11*, 633.

Sharber, J. R. (1981), The continuous (diffuse) aurora and auroral-E ionization, in *Physics of Space Plasma*, vol. 7, edited by T. S. Chang, B. Coppi, and J. R. Jasperse, p. 115, Scientific, Gainesville, Fla.

Solomon, S. C. (2001), Auroral particle transport using Monte Carlo and hybrid methods, *J. Geophys. Res.*, *106*, 107.

Strickland, D. J., R. E. Daniell Jr., J. R. Jasperse, and B. Basu (1993), Transport-theoretic model for the electron-proton-hydrogen atom aurora: 2. Model results, *J. Geophys. Res.*, *98*, 21,533.

Synnes, S. A., F. Søraas, and J. P. Hansen (1998), Monte-Carlo simulations of proton aurora, *J. Atmos. Sol. Terr. Phys.*, *60*, 1695.

X. Fang, J. U. Kozyra, and M. W. Liemohn, Space Physics Research Laboratory, University of Michigan, 2455 Hayward Street, Ann Arbor, MI 48109-2143, USA. (xhfang@umich.edu; jukozyra@umich.edu; liemohn@umich.edu)

S. C. Solomon, High Altitude Observatory, National Center for Atmospheric Research, 3450 Mitchell Lane, Boulder, CO 80301, USA. (stans@ucar.edu)